ELSEVIER

Remote Sensing of Environment 78 (2001) 27–38

Remote Sensing of Environment

www.elsevier.com/locate/rse

Absolute radiometric calibration of Landsat 7 ETM+ using the reflectance-based method

K.J. Thome

Remote Sensing Group, Optical Sciences Center, University of Arizona, 1631 E. University Boulevard, Tucson, AZ 85721, USA

Received 1 June 2000; received in revised form 22 December 2000; accepted 30 April 2001

Abstract

A key to the continuation of quantitative data from the Landsat series of sensors is the radiometric understanding of the sensor. Vicarious calibration methods are one approach that has been used successfully for the absolute radiometric calibration of Thematic Mapper (TM). One of these vicarious methods is the reflectance-based approach that is applied here to the radiometric calibration of the Enhanced Thematic Mapper Plus (ETM+) sensor on the Landsat 7 platform. This method is described for application to ETM+. Results from ground-based measurements of atmospheric conditions and surface reflectance made at Railroad Valley Playa, Nevada, Roach Lake Playa, Nevada, and White Sands Missile Range, New Mexico are presented including descriptions of the test sites. The gains derived from four dates using these sites spanning the period from June 1999 to October 1999 agree to within 5% of each other and to better than 7% with the prelaunch, laboratory-derived gains. This is within the combined 5% uncertainty of the prelaunch values and the estimated 3–5% uncertainty of the reflectance-based method. The gains determined from the reflectance-based method are all lower than the prelaunch values for bands 1–5 and the values for band 7 exceed the prelaunch gains. These biases could be caused by errors in the treatment of atmospheric aerosols at shorter wavelengths and uncertainties in the assumed solar irradiances used to convert the relative radiances to absolute values at longer wavelengths.

Keywords: Absolute radiometric calibration; Vicarious calibration

1. Introduction

The Landsat series of satellites provides the longest running continuous data set of high-spatial resolution imagery dating back to the launch of Landsat 1 in 1972 and continuing with the April 15, 1999 launch of Landsat 7. A large part of the success of the Landsat program can be attributed to the knowledge of the radiometric properties of the Landsat sensors. This knowledge is due to the combination of prelaunch and postlaunch efforts using laboratory, on-board, and vicarious calibration methods (where vicarious calibration refers to any method not relying on on-board calibrators) (Thome, Markham, Barker, Slater, & Biggar, 1997). The radiometric calibration of these systems not only helps characterize the operation of the sensors, but, more importantly, this calibration allows the full Landsat data set to be used in a quantitative sense for such applications as land use and land-cover change.

From a platform standpoint, the Landsat series of satellites can be viewed in two distinct parts. The first includes Landsats 1, 2, and 3 that carried the return beam vidicon (RBV) camera and the Multispectral Scanner System (MSS). The second phase of Landsat includes the subsequent Landsat platforms from Landsats 4 to 7. These platforms have a lower orbit, and have higher spatial and spectral resolution sensors, and a faster repeat cycle. These platforms omitted the RBV cameras but Landsats 4–6 still carried the MSS. Landsats 4 and 5 included the Thematic Mapper (TM) sensor. Details on the design of these early Landsat sensors can be found in Engel and Weinstein (1983), Lansing and Cline (1975), Markham and Barker (1987), and Slater (1980). A great deal of research was done during the early days of Landsat to understand these systems, including the extensive Landsat Image Data Quality Assessment (LIDQA) program (Markham & Barker, 1985). The last two Landsat platforms, Landsats 6 and 7, have included improvements to the TM sensor to give better spatial resolution of the thermal infrared band and to include a high-spatial resolution panchromatic band. Unfortunately,

E-mail address: kurt.thome@opt-sci.arizona.edu (K.J. Thome).

0034-4257/01/$ – see front matter
PII: S0034-4257(01)00247-4

Landsat 6 failed to achieve orbit. The Landsat 7 platform carries only one sensor, the Enhanced Thematic Mapper Plus (ETM+) sensor, having dropped the MSS sensor.

In order to understand the necessity for vicarious calibration approaches for the calibration of ETM+, it is helpful to understand the methods and usefulness of the on-board calibrators of past Landsat sensors. On-board calibration of the MSS and TM used solar- and lamp-based approaches for the solar reflective bands. For Landsats 1–3, the MSS included a partial aperture, partial-path solar calibrator. Data from the solar calibrator on Landsat 1 were problematic because of degradation of the optics (Horan, Schwartz, & Love, 1974). Problems with the attitude control of Landsat 2 made the data difficult to interpret, but the solar calibrators on both Landsats 2 and 3 appeared to operate normally (Lansing, 1986). However, the data from these systems have not been used for absolute radiometric calibration of the MSS sensors because the on-board lamp systems worked well (Lansing, 1986).

The on-board lamp calibrator (also referred to as the internal calibrator or IC) for MSS used a shutter wheel and a pair of redundant, tungsten-filament lamps. Within the shutter wheel is a wedge-shaped neutral density filter that provides variable attenuation as it rotates with the shutter wheel. The shutter wheel also serves the purpose of preventing light from the entrance aperture of MSS reaching the focal plane. The IC used for TM is somewhat different with three lamps rather than one. The image of each lamp filament falls on a different attenuating filter such that eight different irradiance levels can be obtained by varying the choice of lamps. For ETM+, a similar IC is used but the design only uses a single lamp level. In addition to the lamp-based IC, ETM+ has two other on-board calibrators. The first is a return to the direct solar illumination technique with a partial aperture approach using a multifaceted optical device to direct solar energy onto the focal plane. The third on-board calibrator is one that is new to Landsat. It is a full-aperture, full-optical-path solar diffuser (Markham, Barker, Boneyk, Kaita, & Helder, 1996) that is the first implementation of a spaceborne diffuser for absolute radiometric calibration of a high-spatial resolution sensor.

The primary advantage to the on-board calibrators is that a calibration is performed with high-temporal frequency. For MSS, the IC provides data after every other scan, while for TM and ETM+ it is at the end of each scan. The partial aperture solar calibrator on ETM+ provides data once per orbit and the full-aperture solar calibrator on ETM+ is used at least once per month. The stability of the lamps that are part of the IC is also such that variability over several scan lines is quite small. This makes the on-board lamps ideal for examining within scene variability of detectors. Experience with the lamps on the early Landsat systems indicates that large, abrupt changes in the lamp output do not occur. Thus, the lamps are also excellent calibration sources over the period of weeks to months. Though untested for ETM+, the direct solar irradiance and solar diffuser calibrators should have similar stability as the ICs.

One thing that must be kept in mind regarding the on-board calibrators is that they cannot provide a calibration that is of higher accuracy than the preflight, laboratory calibrations. That is, the accuracy of the in-flight, absolute calibration must be worse than the preflight calibration, since the preflight calibration source is used to calibrate the on-board calibrators. This gives good justification for developing a calibration approach that is independent of the preflight calibration. In addition, it is possible that degradation of an on-board calibration system can occur over long periods of time. This degradation is typically difficult to determine without means of an additional independent calibration source. This is the advantage to having the three separate calibration approaches for ETM+, but since two of these methods are essentially untested, there is still a justification for including an additional, well-understood calibration methodology. This additional method is the subject of this work and relies on the vicarious calibration technique referred to as the reflectance-based approach.

Many methods have been proposed and used for the in-flight radiometric calibration of satellite sensors. Hovis, Knoll, and Smith (1985) made one of earliest attempts at vicarious calibration by measuring radiances above a ground target from a high-altitude aircraft to verify the degradation of the response of the Coastal Zone Color Scanner's shorter wavelength bands. Since then, many types of vicarious calibration have been developed. Kaufman and Holben (1993) present a method using large-view angles and molecular scatter to characterize the short-wave visible channels of the Advanced Very High-Resolution Radiometer. Vermote, Santer, Deschamps, and Herman (1992) used a similar approach to calibrate the short-wavelength channels of Systeme Pour l'Observation de la Terre-1, Haute Resolution Visible (SPOT-1 HRV) sensor where the contributions from aerosols and sea-surface reflection were determined from data at longer wavelengths. These two approaches are different from Hovis et al. (1985) in that they do not require in-situ measurements. However, because assumptions are made based on climatology, the results of these methods can suffer from larger uncertainties than those using in-situ methods, though methods without in-situ data can be applied with higher-temporal frequency.

In the late-1980s, the Remote Sensing Group (RSG) at the University of Arizona developed three vicarious techniques of absolute calibration that rely on in-situ measurements. These methods are referred to as the reflectance-, irradiance-, and radiance-based techniques (Biggar, Santer, & Slater, 1990; Slater et al., 1987). These three techniques have been used successfully for the SPOT HRV (Gellman et al., 1993), Landsat 5 TM (Slater et al., 1987; Thome et al., 1993), a Daedalus scanner (Balick, Golanics, Shines, Biggar, & Slater, 1991), and the Airborne Visible and Infrared Spectrometer (Vane et al., 1993). A variation of the radiance-based approach is cross-calibration where the

calibration of one satellite sensor is transferred to other uncalibrated systems. Teillet et al. (1990) and Che et al. (1991) employed this approach to calibrate several of the Advanced Very High-Resolution Radiometers. This method is especially useful for large-footprint sensors for which it is more difficult to apply the reflectance- and irradiance-based approaches.

In this work, the results of the radiometric calibration of the solar-reflective, multispectral bands of ETM+ using the reflectance-based approach are presented. Studies on the calibration of the thermal band of ETM+ can be found elsewhere in this special issue. Results from the panchromatic band are not presented here due to the difficulty in accounting for the broadband spectral response of this band. Future work will evaluate the calibration of this band using reflectance-based methods. The vicarious calibration results shown here rely on ground-based data collected at the RSG's historical test site at White Sands Missile range as well as data collected at dry lake test sites in California and Nevada. Section 2 describes these test sites followed by a description of the reflectance-based measurements made for the current work. The results from this work are then presented showing that the ETM+ sensor does not show any significant degradation during the first 6 months of operation. Section 6 gives areas for future work.

2. Test site descriptions

Vicarious calibration, whether it is the reflectance-, irradiance-, and radiance-based techniques of the RSG or one of many other approaches, requires careful selection of the test site used. For the RSG's work, there are several critical characteristics of an ideal test site and, in brief, these are (Scott, Thome, & Brownlee, 1996) the following.

(1) A high-reflectance site reduces the impact of errors in determining the radiance due to atmospheric scattering. A site reflectance greater than 0.3 ensures that the radiance due to reflection of the direct solar irradiance from the surface is the dominant contributor to the at-sensor radiance.

(2) An elevation of at least 1 km reduces the amount of atmospheric aerosols and the errors associated with predicting their characteristics and concentrations.

(3) High-spatial uniformity over a large area minimizes the effects of scaling the reflectance data to the size of the full test site. The level of uniformity required is difficult to quantify other than to say, ''the more uniform the better.''

(4) Changes with season should be minimal. This implies a site that is free of vegetation. Arid regions typically improve the probability of a temporally stable site, while at the same time increasing the probability of cloud-free days.

(5) The site should be nearly lambertian to decrease uncertainties due to changing solar and view geometry. A flat site has the advantage of reducing BRF effects and eliminating shadow problems.

(6) Spectral uniformity of the site is considered important over as wide a spectral region as possible. This simplifies band integrations and decreases the effects of spectral mismatch between the ground-based and ETM+ sensors.

(7) Accessibility of the site and distance from Tucson are also important factors.

There is no ideal calibration site that satisfies all of the above conditions. In the southwestern United States, there exist several fairly uniform reflectance sites, which have been used over the course of many years by the RSG for calibrations of Landsat-TM, SPOT-HRV, and other airborne and satellite-borne imaging sensors. Three of these test sites were used for the current work and details of these test sites are given below.

2.1. White Sands Missile Range

The White Sands Missile Range test site in New Mexico has been in use for vicarious calibration since the mid-1980s. It is located in the desert southwest of the United States in a region of low aerosol loading and an elevation of 1.2 km. The test site used here for ETM+ is commonly referred to as Chuck Site and is located in the alkali flats region. The coordinates of the test site are 32.919°N latitude and 106.351°W longitude. The site is relatively devoid of vegetation, though the area near the site includes regions of greater vegetation and large gypsum dunes. In the VNIR, the White Sands site has a fairly flat spectral reflectance that is quite high, however, the reflectance is much lower and spectrally structured in the SWIR. The level of reflectance varies with season with the lowest reflectance values occurring during the winter months when portions of the missile range are either underwater or wet from the higher water table. Highest reflectance values are typically seen in late fall after the surface has dried after summer-season rains. The size of the White Sands area is the largest of the test sites with an overall size of about 50 km.

2.2. Railroad Valley Playa

Railroad Valley Playa is a dry lakebed in Nevada with a composition dominated by clay. The coordinates of this test site are 38.504°N latitude and 115.692°W longitude and its site is located at 1.3 km above sea level between the cities of Ely and Tonopah, NV. It is a desert site with no vegetation and aerosol loading is typically low. Railroad Valley Playa is the largest of the playa test sites used by the RSG, but is still about one-fourth of the area of White Sands. While the spectral reflectance of the playa sites is typically lower than that of White Sands, especially in the blue part of the spectrum, the spectral reflectance is reasonably flat throughout the spectral range of ETM+. Temporal records for this site do not exist for as long a period of time as for White Sands, so it is difficult to state how the reflectance varies as a function of time of year. Early indications are that it too has lowest reflectance in the winter months due to a rising

water table. The site is also more susceptible to cloudiness than the White Sands site with peak cloudiness in the winter and late summer months.

2.3. Roach Lake Playa

The Roach Lake Playa test site is at an elevation of 0.8 km located near the California–Nevada border along Interstate 15, which is the major highway between Los Angeles, CA and Las Vegas, NV. The coordinates of the test site are 35.651°N latitude and 115.367°W longitude. This playa is immediately north of another playa, Ivanpah Playa, that is also used by the RSG. The size of Roach Lake is approximately 3×3 km. This is somewhat smaller than the Ivanpah Playa, which is approximately 3×7 km, hence, it is a secondary site for the RSG. Unfortunately, at the time of the work for ETM+, access to the Ivanpah Playa was restricted by the Bureau of Land Management to prevent damage to the playa surface while studies of its use were being made. The spatial uniformity of the Roach Lake test site is the best of the three sites used here but its size is the smallest. Its reflectance has a similar spectral shape as that of Railroad Valley, but is significantly brighter than Railroad Valley while darker than White Sands in the visible and near infrared. Since this marked the first time that Roach Lake was used, the temporal stability of the reflectance is not understood at this time. Work at Ivanpah Playa shows that this playa's reflectance is quite stable with time except for the few days following heavy rainfall.

3. Reflectance-based approach

This section gives details of the reflectance-based method used in this work. The four sections describe the basic parts of this approach. Uncertainties in the results of these measurements are discussed in a later section.

3.1. Surface reflectance retrieval

The reflectance-based approach relies on ground-based, surface reflectance measurements of a selected site. For ETM+, this site is a rectangular area that is 480×120 m with the long side of the site oriented approximately in the along-track direction of Landsat 7. This is the size that was originally selected by the RSG for work with Landsats 4 and 5 TMs and ensured that all 16 detectors of the multispectral bands were sampled as well as all of the detectors for the thermal bands. This means that four ground samples for each of the 16 multispectral detectors are collected corresponding to the nominal 30-m ground spatial resolution of the multispectral bands. Changing the size of the site to a larger size would provide more statistical sampling for each detector, but increasing the size also causes the data collection to take longer. This can then create problems due to changes in solar zenith angle causing bidirectional reflectance effects and a longer data collection time increases the probability that changes in atmospheric conditions can lead to changes in the downwelling irradiance on the surface. Selecting a smaller site would either mean sampling fewer pixels in the cross-track direction or fewer detectors. In addition, this would mean having different sized sites than used for ongoing work with TM.

To obtain the reflectance of the test site, a spectroradiometer is transported across the entire site. The primary instrument for the surface-reflectance collection is a commercially available spectrometer that gives 1.4-nm spectral resolution from 350 to 1000 nm and 10-nm resolution for the 1000- to 2500-nm spectral range. The output from the spectroradiometer is interpolated within the data collection software to report results at a 1-nm spacing across the entire spectral range. The instrument is transported across the site using a backpack device that extends the instrument away from the body of the user and raises the foreoptics to a height of about 2 m above the ground. An 8° field of view is used for the measurements giving a circular sample on the ground of approximately 0.3 m in diameter. A larger field of view would give better spatial sampling but would be more susceptible to surface bidirectional reflectance effects. A smaller field of view forces a longer integration time, and thus increases the time needed to measure the test site. The user walks a path parallel to the cross-track direction of Landsat 7 through the center of the four cross-track pixels for all 16 along-track pixels. The spectroradiometer is configured to average 30 spectra per sample and 10 samples are collected within a single "pixel." This gives a total of 19,200 spectra collected over the site and 640 samples. In essence, this means that approximately 1400 m^2 is sampled by the reflectance measurements. Considering that the site is 57,600 m^2 in size, it should be clear that either a homogeneous or randomly varying site is needed since measurements of $<2.5\%$ of the site area are used to represent the entire area. It takes 45–60 min to collect these data when the reference measurements are included.

Reflectance of the site is determined by ratioing the measurements described above to those of a reference panel for which the bidirectional reflectance factor has been determined in the laboratory. Measurements of the reference are made at the start and end of the data collection, as well as after every eight pixels (or, equivalently, every 80 test-site samples). This level of sampling reduces the level of uncertainty due to changes in instrument response with time and changing atmospheric conditions, while keeping the data collection time to a reasonable level. Knowing the bidirectional reflectance of the reference allows the reflectance of each sample to be computed taking into account effects due to sun-angle changes and reflectance panel bidirectional reflectance over the 60 min of data collection. Global, downwelling irradiance data are also collected near the test site to determine if there are significant changes in diffuse skylight illumination during the measurement

period. Once each of the spectral samples of the site is converted to reflectance, all 640 data points are averaged to give a single spectral reflectance for the entire site.

It should be clear that a critical part of this reflectance retrieval is the characterization of the reference panel in the laboratory. The calibration of this panel is done with reference to a standard made from pressed polytetrafluoroethylene based on a prescribed approach defined by National Institute of Standards and Technology (NIST) (Biggar et al., 1988). The calibration reference is a directional-to-hemispheric reflectance standard provided by NIST. Polynomial fits are made to the measured data to calculate the reflectance of the field standard for the sun-view geometry and wavelengths for a given set of field measurements (Biggar et al., 1988). Past work relied on Halon as the standard of diffuse reflectance, but Halon is no longer available. Spyak and Lansard (1997) investigated another polytetrafluoroethylene powder, Algoflon F6, and found it to be a suitable replacement and this is currently being used.

3.2. Atmospheric characterization

Atmospheric characterization data are collected at the same time as the surface reflectance measurements. This characterization relies on solar extinction measurements from a 10-band solar radiometer (Ehsani, Reagan, & Erxleben, 1998). The solar radiometer is relatively calibrated immediately prior to, during, or after each field campaign. Data are used in a Langley method retrieval scheme to determine spectral atmospheric optical depths (Gellman, Biggar, Slater, & Bruegge, 1991). The optical depth results are used as part of an inversion scheme to determine ozone optical depth and an aerosol size distribution (Biggar, Gellman, & Slater, 1990). In this work, the aerosols are assumed to follow a power law distribution, also referred to as a Junge distribution. The advantage to such a distribution is that it requires only one number to define the aerosol size distribution, the so-called Junge parameter. Optical depths at 1-nm intervals from 350 to 2500 nm are computed from this derived size distribution (Junge parameter) and columnar ozone. Columnar water vapor is derived from the solar extinction data using a modified Langley approach (Thome, Herman, & Reagan, 1992).

3.3. Radiative transfer code

These atmospheric and surface data are inputs to a radiative transfer code that computes hyperspectral, at-sensor radiances (Thome et al., 1996) based on a Gauss–Seidel iteration approach (Herman & Browning, 1965). The code assumes a plane-parallel homogeneous atmosphere and divides this atmosphere into layers to account for the vertical distribution of scatterers and weak absorption due to ozone in the visible and near infrared (approximately the 400- to 800-nm spectral range know as the Chappuis absorption band). The Junge parameter described in Section 3.2 that is derived from the solar radiometer measurements is used to compute Mie scattering phase functions used in the code. While the radiative transfer code can include nonlambertian effects of the surface, bidirectional reflectance measurements of the surface were not available for this work, so the surfaces are assumed to be lambertian.

Strong gaseous absorption effects due to water vapor are determined using MODTRAN3 to compute transmittance for the sun-to-surface-to-satellite path for 1-nm intervals from 350 to 2500 nm (Berk, Bernstein, & Robertson, 1989). This sun-to-ground-to-sensor transmittance is multiplied by the at-sensor radiance output from the radiative transfer code to correct the radiances for this strong absorption. While this approach is an approximation that excludes interactions between diffusely scattered radiances and absorption, it does not cause large uncertainties for application to ETM+ because of the small effect of absorption within the ETM+ bands and the high surface reflectance of the test sites used in this work.

The relative radiances that are the output of the radiative transfer code are converted to absolute radiances by multiplying by a supplied solar irradiance curve corrected for changes in earth–sun distance. The solar irradiance standard used in this work is that from MODTRAN3. These absolute radiances are then band-averaged over the ETM+ spectral responses to obtain band-averaged, at-sensor radiances.

3.4. Determination of image digital numbers (DNs) and gain

The final step needed to determine the sensor gain is to compare the DN output from ETM+ to the predicted radiances. The DN output is determined by averaging the output for the 64 pixels related to our ETM+ test site. Level 0R data are used in this work to reduce effects due to resampling of the image data. Because the Level 0R data do not have a geometric correction applied, it is necessary to perform a rudimentary geometric correction of the region near our site. This is done by first locating our test site in the image by finding blue tarpaulins that were laid out at opposing corners of the site. The tarpaulins darken the pixels that contain them and serve as ground control points in the imagery. Using these tarpaulins and also linear features in the image, we linearly shift the pixels in the Level 0R data to find the 64 pixels in the image corresponding to the surface reflectance measurements.

The DNs from these 64 pixels are then averaged and ratioed to the predicted radiance from the radiative transfer code to obtain the gain for the selected band using (Eq. (1)):

$$G_\lambda = \frac{\overline{\mathrm{DN}_\lambda} - O_\lambda}{\langle L \rangle_\lambda} \tag{1}$$

where G_λ is the gain for the given spectral band in units of DN/[W/(m^2 sr μm)], DN_λ is the average DN for the

Table 1
Average atmospheric conditions for 10-min period about the given overpass time for each of the four calibration dates

Date (1999)	Overpass time (MST)	550-nm aerosol optical depth	Junge parameter	Column ozone (cm-atm)	Column water vapor (cm)
June 1	11:17	0.1024	3.112	0.172	1.139
July 20	11:08	0.0325	2.970	0.250	1.595
October 8	11:09	0.0381	3.093	0.187	1.135
October 20	10:32	0.0207	3.264	0.235	0.758

spectral band based on the 64 pixels, O_λ is the offset in DN from the calibration file, and $\langle L_\lambda \rangle$ is the band-averaged spectral radiance predicted at the sensor from the radiative transfer code.

4. Recent Landsat 7 ETM+ results

The results presented here are from three separate calibration sites for four separate dates spanning the time period from May to October 1999. In addition to the four data sets presented here, campaigns to White Sands Missile Range on May 21 and 26, Ivanpah Playa on May 22, Roach Lake Playa on September 22, and Railroad Valley Playa on May 27 and July 27 were also attempted. All of the data collections in May were during the initial checkout period of the ETM+ sensor. Thus, the orbit of the sensor was not that of the Worldwide Reference System path/row and Landsat 7 was not at its final 705-km orbit. While this created some difficulties because of the different sensor inclination and oversampling due to the lower orbit, it also allowed multiple calibration attempts at test sites without having to wait for the 16-day repeat cycle. The ground-based data collections from May 21 and 26 during this checkout period were successful, however, the reflectance of the White Sands test site was such that all bands of ETM+ were saturated. The surface data collection for May 22 was also successful, but, unfortunately, the imagery from the ETM+ sensor was one of the few data sets lost during the checkout period. The May 27, July 27, and September 22 data sets were contaminated by clouds. This is an indication of the difficulties of vicarious calibration using in-situ measurements. Of 10 total data collection attempts, only four high-quality data sets were obtained and problems will sometimes be encountered with weather-related difficulties and the vagaries of the sensor.

4.1. June 1 — Railroad Valley Playa

The first successful data collection by the RSG with both a combination of clear skies and successful image acquisition was June 1 at the Railroad Valley Playa. The weather on this date was mostly cloudy in the morning with clearing skies. There were cumulus clouds visible throughout the sky at the time of overpass, but no clouds were over the site at overpass, nor was the sun obstructed for the overpass time shown in Table 1. Further indication of the atmospheric conditions can be seen in Fig. 1 showing pyranometer data scaled to fit on the same graph as the optical depth data that are also shown. These pyranometer data give a qualitative measurement of the downwelling total irradiance and large, abrupt changes in the output are indicative of clouds covering the sun. Clouds in other parts of the sky are indicated by smaller scale fluctuations in the irradiance.

Also shown in Fig. 1 are the inferred aerosol optical depths at 550 nm. These are obtained using the methods described in Section 3. The data give both an indication of the level of turbidity of the atmosphere as well as its temporal stability and these data clearly show the variable nature of the sky early in the day, while the period around overpass was clear and temporally stable. Table 1 gives the average optical depth at 550 nm for a 10-min time period about the overpass time of ETM+. Also given are the average Junge parameter, column ozone, and column water vapor derived from the solar extinction measurements. While it is clear that the early morning and late afternoon atmospheric conditions were cloudy, the standard deviation of the 10-min averages were all less than the expected uncertainties in the derived quantities, implying that atmospheric variability is a small contributor to any

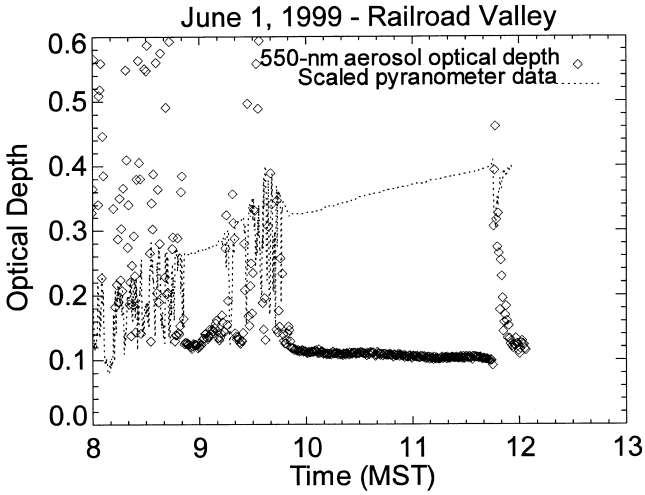

Fig. 1. Aerosol optical depth at 550 nm inferred from solar extinction measurements from Railroad Valley on June 1, 1999. Also shown for reference are scaled pyranometer data to indicate downwelling global irradiance.

uncertainties. All of the values shown in Table 1 are typical of our test sites, although the optical depth on this date is higher than normal. However, it is still quite low when compared to values from more typical areas around the world.

The other component to the reflectance-based method is the retrieved surface reflectance at the time of overpass. Fig. 2 shows the spectral reflectance derived for the test site on this date. In addition, the standard deviation of this average is shown as a percent of the average reflectance. The average reflectance shown is that of all data collected during a 60-min period about the ETM+ overpass time. As mentioned previously, the pyranometer and optical depth data shown in Fig. 1 indicate quite a bit of atmospheric variability early in the day and later in the day after overpass. However, the period during which the surface reflectance data were collected was stable enough that no corrections for atmospheric variability were made in the retrieved reflectance. Table 2 presents the band-averaged reflectance for each of the six multispectral bands of ETM+ derived from the spectral reflectance curve in Fig. 2.

Gaps seen in the reflectance and standard deviation curves are regions of the spectrum strongly affected by water vapor absorption. Hence, the spectroradiometer measurements suffer from poor signal-to-noise effects in these spectral regions. This can be seen somewhat in the graph around the 940-nm water vapor absorption feature (it is more noticeable in related figures for the other test sites in Figs. 4 and 5). While the spectral reflectance in this part of the spectrum looks reasonable, the noisiness of the data is larger than in other parts of the spectrum. This is due to a combination of three separate factors. The first is that the absorption reduces the incident solar irradiance in this part of the spectrum reducing the measured signals and hence the signal-to-noise-ratio of the instrument. The second factor is similar in nature. It is due to the fact that

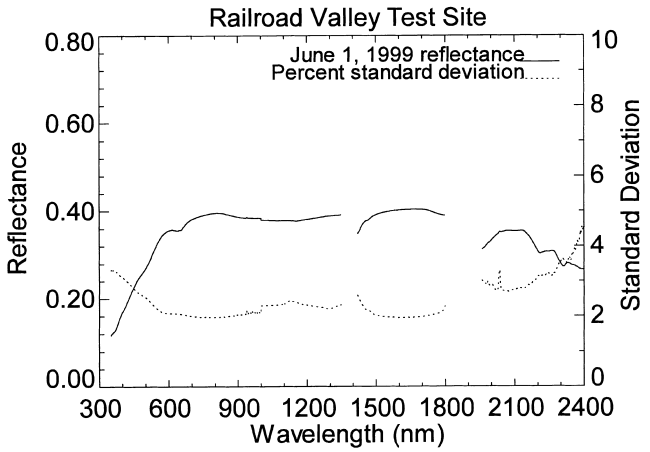

Fig. 2. Spectral reflectance results for Railroad Valley Playa site for June 1, 1999.

Table 2
Summary of retrieved surface reflectance results for all seven bands

Date (1999)	Band 1	Band 2	Band 3	Band 4	Band 5	Band 7
June 1	0.253	0.332	0.365	0.393	0.402	0.318
July 20	0.274	0.397	0.493	0.550	0.632	0.583
October 8	0.260	0.375	0.468	0.517	0.580	0.528
October 20	0.480	0.559	0.602	0.645	0.454	0.170

the silicon-based detector of the spectroradiometer has poorer response at these wavelengths, again leading to poorer signal to noise. The abrupt change in the percent standard deviation at 1000 nm is due to a change in the spectroradiometer to a different detector that has better response than silicon at these wavelengths. The third cause of larger standard deviations is due to changes in the column water vapor amounts between the measurements. This is especially important when considering differences in water vapor amounts between the reference panel measurements and the site measurements. This factor is considered to be small in this case due to the temporal stability of the retrieved water vapor amounts from the solar extinction data.

Also seen in Fig. 2 is an increase in the percent standard deviation at shorter wavelengths. This is due to the fact that the spatial homogeneity of the surface is relatively constant with wavelength in reflectance units. That is, if the reflectance at 600 nm decreases by 0.02 in reflectance, then there is a similar decrease in reflectance at other wavelengths. Because the reflectance of the surface decreases at shorter wavelengths, this leads to a larger percent standard deviation. A similar effect is seen at these wavelengths for measurements at Roach Lake and at longer wavelengths at White Sands Missile Range.

The results of these measurements were used as inputs to the radiative transfer code. Table 3 gives the predicted at-sensor radiances for each of the bands considered here as well as the average DNs determined from the imagery. The uncertainty for the DNs given in the table is the $1-\sigma$ standard deviation of the average of the 64 pixels corresponding to the test site used. In addition, the table also contains the minimum and maximum average DNs determined by shifting the 64-pixel area by one pixel in all directions. This gives an indication of the uncertainty due to a misregistration between the ground-based reflectance data and the imagery. The differences caused by misregistration are all $<1\%$, while the percent standard deviation of the 64-pixel average is approximately the same as that of the percent standard deviation of the reflectance data.

Finally, combining the data in Table 3 allows for the sensor gain to be computed. The units used here are in DN per unit radiance with radiance having the units of W/[m^2 sr μm]. The values for each of the multispectral bands is given in Table 4. The table also includes the prelaunch, laboratory-derived gains for reference.

Table 3
Site digital number results for each band and each date examined. Also shown are the predicted radiances from the reflectance-based method for each date and band.

		Band 1	Band 2	Band 3	Band 4	Band 5	Band 7
June 1	Average site DN	194.4	201.8	242.1	178.1	194.5	156.1
	$1-\sigma$ S.D.	2.5	2.7	3.3	2.1	2.5	2.6
	Minimum DN	193.6	199.9	239.8	176.6	192.9	154.8
	Maximum DN	195.3	202.9	243.6	179.1	195.6	156.8
	Radiance (W/[m^2 sr μm])	153.7	168.5	152.7	109.8	24.61	6.038
July 20	Average site DN	203.3	231.2	255.0	234.1	255.0	254.0
	$1-\sigma$ S.D.	3.6	3.4	–	2.3	–	1.5
	Minimum DN	202.9	230.8	255.0	233.9	255.0	253.1
	Maximum DN	203.6	231.6	255.0	234.6	255.0	254.3
	Radiance (W/[m^2 sr μm])	161.9	193.7	200.4	150.1	37.84	10.70
October 8	Average site DN	157.7	176.6	235.6	180.0	212.7	190.2
	$1-\sigma$ S.D.	3.4	3.9	5.2	3.6	3.5	4.1
	Minimum DN	156.9	176.0	234.9	179.4	212.1	189.3
	Maximum DN	158.7	177.8	236.4	180.7	213.7	191.0
	Radiance (W/[m^2 sr μm])	125.1	148.7	153.7	114.5	28.15	7.82
October 30	Average site DN	240.0	237.2	255.0	210.5	160.7	68.8
	$1-\sigma$ S.D.	5.1	5.5	0.0	4.6	3.3	1.8
	Minimum DN	239.4	236.5	255.0	210.0	160.7	68.6
	Maximum DN	241.0	238.2	255.0	211.5	161.2	69.0
	Radiance (W/[m^2 sr μm])	194.1	198.3	181.2	133.8	20.62	2.365

4.2. July 20 — Roach Lake Playa

The weather on this date was clear with no clouds. Fig. 3 shows the derived 550-nm optical depth as a function of time for this date, as well as the scaled pyranometer data. This graph is similar to that of Fig. 1, except the *y*-axis scale is one order of magnitude smaller. It is clear from this figure that the atmosphere was quite stable during the entire period of measurement as well as the time around sensor overpass. The atmospheric results are summarized in Table 1. Fig. 4 shows the spectral reflectance derived for the test site on this date in a similar fashion to Fig. 2. By comparison, the spectral curves are similar in shape, but Roach Lake is clearly brighter, as can also be seen in Table 2. Also evident in the figure is the lower percent variability of the site. Table 3 summarizes the results of this collection for each spectral band considered here, as well as the DNs derived from the Level 0R image data. One problem that was encountered for this data collection was the saturation of bands 3 and 5 and saturation of some pixels in band 7. Thus, it is not possible to calculate gains for these bands on this date. The retrieved gains from this campaign are given in Table 4.

Table 4
Derived gains for each of the four dates and the six visible and near-infrared multispectral bands of ETM+ (values for April 15 indicate prelaunch, laboratory-derived gains)

	Gains [DN/(W/(m^2 sr μm))]					
Date (1999)	Band 1	Band 2	Band 3	Band 4	Band 5	Band 7
April 15	1.22	1.18	1.51	1.51	7.59	21.75
June 1	1.167	1.108	1.487	1.486	7.294	23.370
July 20	1.163	1.116	–	1.560	–	–
October 8	1.141	1.087	1.435	1.441	7.024	22.410
October 30	1.159	1.121	–	1.462	7.067	22.751

Values also determined after removing 15-DN offset for all bands and dates.

4.3. October 8 — Roach Lake Playa

Conditions on October 8 at Roach Lake were very similar to those on July 20. Table 1 summarizes the atmospheric results and Table 2 the reflectance data. From Table 2, it is clear that the surface of the playa is somewhat darker with the reflectance in the visible and near-infrared about 5% darker while the short-wave infrared darkened

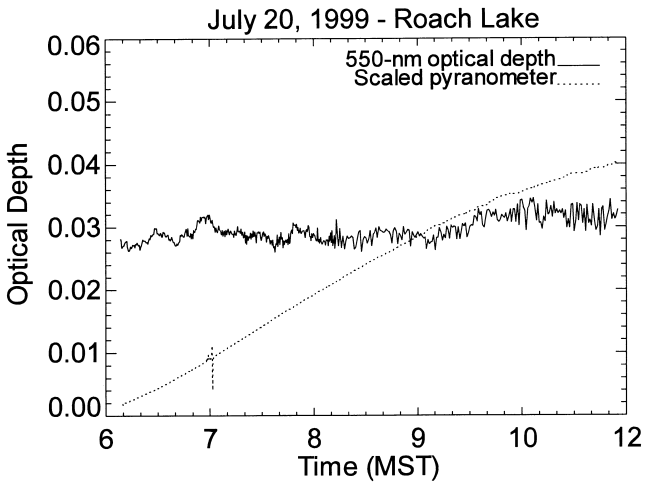

Fig. 3. Aerosol optical depth at 550 nm inferred from solar extinction measurements from Roach Lake on July 20, 1999. Also shown for reference are scaled pyranometer data to indicate downwelling global irradiance.

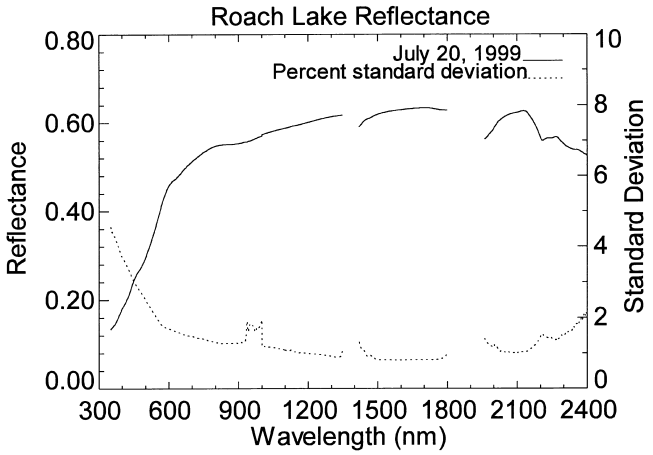

Fig. 4. Spectral reflectance results for Roach Lake site for July 20, 1999.

slightly more (8–9%). Much of this was due to recent rainfall in the area that had left standing water over portions of the playa. The DNs retrieved from imagery are given in Table 3. Here, it is clear that the site was less homogeneous than for the previous date. However, the level of inhomogeneity is still <2% and not a large source of uncertainty. The retrieved gains from this campaign are given in Table 4.

It should be noted that the reflectance results from this date are an excellent example of the need for ground-based measurements at the time of sensor overpass to characterize the surface reflectance of the test site. While the surface reflectance of the sites used by the RSG has low variability with time, the 5–9% change in reflectance would have a similar effect on the predicted at-sensor radiance. Thus, using the retrieved reflectance values from July 20 would lead to a 5–9% error in the retrieved gain and this is unacceptable when attempting to absolutely calibrate a sensor to better than 5%. This effect has been well known from the RSG's work at White Sands Missile Range where the test site's reflectance has been known to vary by more than 20% depending upon the time of year (Thome et al., 1993).

4.4. October 30 — White Sands Missile Range

The final data set presented here uses data from White Sands Missile Range at the RSG's Chuck Site area. Weather on this date was similar in nature to that of the Roach Lake data sets. The retrieved atmospheric conditions are summarized in Table 1 and show that conditions were indeed similar to those of July 20 and October 8. Fig. 5 shows the spectral reflectance derived for the test site along with the percent standard deviation of the average. The large spectral variability of the reflectance in the short wave is a clear indication for selecting the dry-lake test sites for vicarious calibration. In addition, Fig. 5 shows the surface to be less homogeneous, and the reflectance in the short-wave infrared is much lower than for the playa sites. As described in the discussion for Fig. 2, this decrease in reflectance in the short-wave infrared then leads to much larger percent standard deviations at these wavelengths. The band-averaged reflectance for this campaign is given in Table 2. Table 3 summarizes the average DNs for the site and the predicted at-sensor radiances, and Table 4 gives the retrieved gains from this campaign.

4.5. Discussion

Examining Table 4 leads to two key conclusions. The first is that the agreement between different dates is quite good with the range of gains being <3.5% for all bands. This implies two things. The first is that the response of the ETM+ sensor was stable during this time period. The second is that the precision of these results is quite good, giving confidence that trends in instrument response could be determined given enough data points. The second conclusion is that the vicarious results agree well with the prelaunch gains. The estimated $1-\sigma$ uncertainty in the prelaunch values have been given as 5% absolute (B. Markham, personal communication), and, as will be discussed in Section 5, the estimated uncertainties in the vicarious calibrations are 3–5%. Thus, the vicarious calibration results agree to better than the combined uncertainties in the two methods. An obvious interpretation of this result is that the prelaunch calibration for ETM+ is still valid for this time period.

It should be noted that while the results of the prelaunch calibration and the postlaunch vicarious calibration agree to within their combined uncertainties, there appears to be biases between the results. The vicarious results for bands 1–5 are all less than the prelaunch value (except for the value obtained for band 4 on July 20), while the vicarious results for band 7 give gain values that are higher than the prelaunch. It is not clear, at this point, what is the cause of this difference, but work is currently underway to understand these "biases."

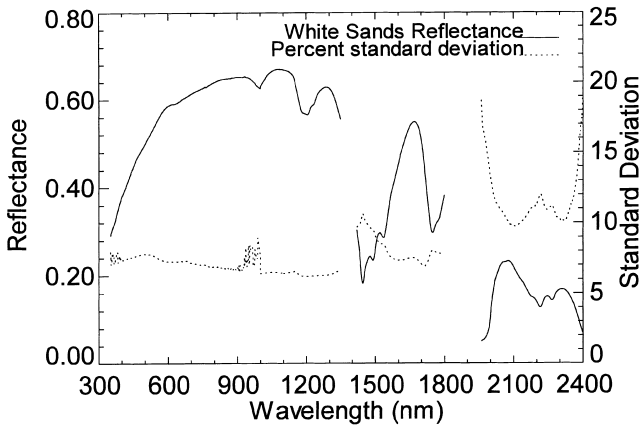

Fig. 5. Spectral reflectance results for White Sands Missile Range for October 30, 1999.

5. Uncertainties

There are two ways in which to view the uncertainties of the results. One way is to determine the uncertainties of each separate field measurement and then determine how these uncertainties impact the predicted at-sensor radiances. The other is to compare independently derived results from several groups measuring the same site at the same time and produce results for identical spectral bands. Results of both approaches have been presented previously and, since this earlier work is still valid for application to ETM+, they are only summarized here (Biggar, Gellman, & Slater, 1994; Thome et al., 1998).

From the description of the reflectance-based method given earlier, it can be seen that there are four basic areas of uncertainty in the method: (1) atmospheric characterization, (2) surface characterization, (3) radiative transfer code, and (4) computation of the site-average DNs. The factors leading to uncertainties in determining the site average DN are an incorrect determination of the site's location in the image and the subsequent misregistration of the site's surface reflectance to DN. As discussed in Section 3, the use of tarpaulins allows us to determine the location of our site to better than one pixel. Even allowing a misregistration of up to two pixels leads to less than a 1% uncertainty in the site-averaged DNs and thus the computation of the calibration coefficient. Uncertainties caused by the radiative transfer code are its inherent numerical accuracy and assumptions. Biggar et al. (1994) lists the uncertainty due to these as $<1\%$ in the top-the-atmosphere radiance computed by the code for cases when the radiative transfer codes are used with identical atmospheric assumptions and inputs.

The uncertainties in the retrieved reflectance are harder to quantify since there are two errors to consider here. The first is the error in an individual measurement, that is, the accuracy of a single reflectance measurement. The uncertainty in a single measurement of the site reflectance is $<2\%$ for the range of reflectances seen at our field sites (that is a reflectance value of 0.01 at a reflectance of 0.50). The primary uncertainty sources for the surface reflectance retrieval are the calibration of our field reference panels, instrument noise of our field radiometers, and diffuse skylight corrections. Recall that these individual reflectances are averaged to determine an overall site reflectance. The uncertainty due to this can be evaluated by resampling the reflectances that are used to determine the site reflectance. Randomly removing as many as one-half of the samples from the averaging has less than a 1% effect on the retrieved reflectance. Thus, while the small-scale variability of the surface reflectance of these sites can be quite large, as evidenced by the large standard deviations of the site averages, this variability is random enough that it does not represent the uncertainty of the retrieved reflectance.

The last area of uncertainty is the atmospheric characterization. Much of our uncertainty here is due to an incorrect determination of the aerosol type, both the aerosol size distribution and the aerosol complex index of refraction. These two parameters lead to top-of-the-atmosphere-radiance uncertainties of 2.0% and 2.5%, respectively. If it is assumed that the above errors are independent, then a root-sum square approach leads to an overall uncertainty of 5%.

To help evaluate this estimated accuracy, a joint field campaign to Lunar Lake Playa was organized under support from NASA's EOS project (Thome et al., 1998). This international campaign included scientists from three sensors on the EOS Terra Platform, the ETM+ sensor, and other non-EOS investigators. This campaign pointed out differences between groups in the order of 5% in the spectral region corresponding to the bands of ETM+. Most of the differences seen were attributed to several groups using directional–hemispherical reflectances and other groups using directional–directional reflectances for the reflectance of their reflectance panels. When these differences were taken into account, even better agreement was found. It should be pointed out that these differences are more an indication of the precision of the vicarious calibration rather than the accuracy, since many of the groups used very similar retrieval algorithms (for example, the assumption of a Junge size distribution and use of similar reflectance references). However, the comparisons included a variety of radiative transfer codes, atmospheric instrumentation, and surface reflectance data collection techniques and equipment. Thus, this comparison is a good indication that the uncertainties of the vicarious calibrations is lower than 5%. One last point, however, is that the above cross-comparisons were made on the relative at-sensor radiances. An additional uncertainty is added when converting these relative radiances to absolute radiances.

6. Conclusions

Four separate vicarious calibration campaigns were held for the purpose of evaluating the responsivity of the solar-reflective, multispectral bands of the Landsat 7 ETM+ sensor. These campaigns took place early in the mission with the first set of results obtained 47 days after launch. The final data set shown here was collected 198 days after launch. The vicarious results agreed with each other to better than 3.5% indicating both the stability of the ETM+ sensor and the quality of the vicarious results.

Past work with the reflectance-based method used here indicate that the method has absolute uncertainties in the 3–5% range. Comparisons of the reflectance-based results to the prelaunch, laboratory-based gains agree to better than 7% in all cases, which is within the combined uncertainties of the two approaches. Further work is needed to better understand the possibility of biases between the prelaunch and vicarious methods since the reflectance-based values for bands 1–5 are less than those from prelaunch and the values for band 7 exceed the prelaunch. A possible source of the bias could be incorrect

assumptions about aerosol absorption and this would strongly affect the shorter wavelength bands. Biases at the longer wavelengths could be due to uncertainties in the assumed solar irradiances used to convert the relative radiances to absolute values. Further work will also include comparisons to the on-board calibrators of ETM+ to better understand the accuracy of the vicarious results and further understand these possible biases.

Future work with the ETM+ sensor related to these vicarious approaches includes the implementation of the irradiance- and radiance-based approaches. In addition, cross-calibration attempts will be made using sensors on-board NASA's Terra platform launched in December 1999. This platform is in an orbit that is 30 min behind Landsat 7, providing comparisons with the sensors on the Terra platform. Because of the excellent quality of the ETM+ data, it should be possible to improve the vicarious methods that are being implemented for the Terra platform to create a quantitatively consistent data set.

Acknowledgments

The author wishes to acknowledge the Atmospheric Sciences Laboratory at WSMR for the use of the site and data support at White Sands, the Bureau of Land Management offices in Tonopah, NV and Needles, CA for their help in accessing our test sites in California and Nevada. I would also like to acknowledge the many students and staff who helped with the field collections used for this work — Arsalan Ahmad, Nik Anderson, Wayne Barber, Xiancheng Ding, Ann Gordon, Hyunki Kim, Rob Kingston, Keith Krause, Michele Kuester, Brian Magi, Marek Mienko, John LaMarr, Prabal Nandy, and Emily Whittington. This research was supported by NASA grant NAG5-2448.

References

Balick, L. K., Golanics, C. J., Shines, J. E., Biggar, S. F., & Slater, P. N. (1991). The in-flight calibration of a helicopter-mounted Daedalus multispectral scanner. *Proceedings of SPIE*, *1493*, 215–223.

Berk, A., Bernstein, L. S., & Robertson, D. C. (1989). MODTRAN: a moderate resolution model for LOWTRAN7. GL-TR-90-0122. Technical Report. Geophysics Directorate, Phillips Laboratory, Hanscom, AFB, MA.

Biggar, S. F., Gellman, D. I., & Slater, P. N. (1990). Improved evaluation of optical depth components from Langley plot data. *Remote Sensing of Environment*, *32*, 91–101.

Biggar, S. F., Gellman, D. I., & Slater, P. N. (1994). Uncertainties in the in-flight calibration of sensors with reference to measured ground sites in the 0.4 to 1.1 μm range. *Remote Sensing of Environment*, *48*, 245–252.

Biggar, S. F., Labed, J. F., Santer, R. P., Slater, P. N., Jackson, R. D., & Moran, M. S. (1988). Laboratory calibration of field reflectance panels. *Proceedings of SPIE*, *924*, 232–240.

Biggar, S. F., Santer, R. P., & Slater, P. N. (1990). Irradiance-based calibration of imaging sensors. *International Geoscience and Remote Sensing Symposium*, *1*, 507–510 (College Park, MA).

Che, N., Grant, B. G., Flittner, D. E., Slater, P. N., Biggar, S. F., Jackson, R. D., & Moran, M. S. (1991). Results of calibrations of the NOAA-11 AVHRR made by reference to calibrated SPOT imagery at White Sands N.M.. *Proceedings of SPIE*, *1493*, 182–194.

Ehsani, A. R., Reagan, J. A., & Erxleben, W. H. (1998). Design and performance analysis of an automated 10-channel solar radiometer instrument. *Journal of Atmospheric and Oceanic Technology*, *15*, 697–707.

Engel, J., & Weinstein, O. (1983). The Thematic Mapper — an overview. *IEEE Transactions on Geoscience and Remote Sensing*, *GE-21*, 258–265.

Gellman, D. I., Biggar, S. F., Dinguirard, M. C., Henry, P. J., Moran, M. S., Thome, K. J., & Slater, P. N. (1993). Review of SPOT-1 and -2 calibrations at White Sands from launch to the present. *Proceedings of SPIE*, *1938*, 118–125.

Gellman, D. I., Biggar, S. F., Slater, P. N., & Bruegge, C. J. (1991). Calibrated intercepts for solar radiometers used in remote sensor calibration. *Proceedings of SPIE*, *1493*, 175–180.

Herman, B. M., & Browning, S. R. (1965). A numerical solution to the equation of radiative transfer. *Journal of Atmospheric Science*, *22*, 559–566.

Horan, J. J., Schwartz, D. S., & Love, J. D. (1974). Partial performance degradation of a remote sensor in a space environment and some possible causes. *Applied Optics*, *13*, 1230–1237.

Hovis, W. A., Knoll, J. S., & Smith, G. R. (1985). Aircraft measurements for calibration of an orbiting spacecraft sensor. *Applied Optics*, *24*, 407–410.

Kaufman, Y. J., & Holben, B. N. (1993). Calibration of the AVHRR visible and near-IR bands by atmospheric scattering, ocean glint, and desert reflection. *International Journal of Remote Sensing*, *14*, 21–52.

Lansing, J. C. (1986). Solar calibration performance in Landsat multispectral scanners. *Applied Optics*, *25*, 333–334.

Lansing, J. C., & Cline, R. W. (1975). The four- and five-band multispectral scanners for Landsat. *Optical Engineering*, *14*, 312–322.

Markham, B. L., Barker J. L. (Eds.) (1985). *Special issue: LIDQA final symposium, Photogrammetric Engineering and Remote Sensing 51,* 1245–1493.

Markham, B. L., & Barker, J. L. (1987). Radiometric properties of US processed Landsat MSS data. *Remote Sensing of Environment*, *22*, 39–71.

Markham, B. L., Barker, J. L., Boncyk, W. C., Kaita, E., & Helder, D. L. (1996). Landsat-7 Enhanced Thematic Mapper Plus in-flight radiometric calibration. *International Geoscience and Remote Sensing Symposium*, *2*, 1270–1272 (Lincoln, NE).

Scott, K. P., Thome, K. J., & Brownlee, M. R. (1996). Evaluation of the Railroad Valley Playa for use in vicarious calibration. *Proceedings of SPIE Conference*, *2818*, 158–166.

Slater, P. N. (1980). *Remote sensing: optics and optical systems* (pp. 465–509). Reading, MA: Addsion-Wesley Publishing.

Slater, P. N., Biggar, S. F., Holm, R. G., Jackson, R. D., Mao, Y., Moran, M. S., Palmer, J. M., & Yuan, B. (1987). Reflectance- and radiance-based methods for the in-flight absolute calibration of multispectral sensors. *Remote Sensing of Environment*, *22*, 11–37.

Spyak, P. R., & Lansard, C. (1997). Reflectance properties of pressed Algoflon F6: a replacement reflectance-standard material for Halon. *Applied Optics*, *36*, 2963–2970.

Teillet, P. M., Slater, P. N., Ding, Y., Santer, R. P., Jackson, R. D., & Moran, M. S. (1990). Three methods for the absolute calibration of the NOAA AVHRR sensors in-flight. *Remote Sensing of Environment*, *31*, 105–120.

Thome, K. J., Gellman, D. I., Parada, R. J., Biggar, S. F., Slater, P. N., & Moran, M. S. (1993). In-flight radiometric calibration of Landsat-5 Thematic Mapper from 1984 to present. *Proceedings of SPIE*, *1938*, 126–131.

Thome, K. J., Gustafson-Bold, C. L., Slater, P. N., & Farrand, W. H. (1996). In-flight radiometric calibration of HYDICE using a reflectance-based approach. *Proceedings of SPIE Conference*, *2821*, 311–319.

Thome, K. J., Herman, B. M., & Reagan, J. A. (1992). Determination of

precipitable water from solar transmission. *Journal of Applied Meteorology*, *31*, 157–165.

Thome, K., Markham, B., Barker, J., Slater, P., & Biggar, S. (1997). Radiometric calibration of Landsat. *Photogrammetric Engineering and Remote Sensing*, *63*, 853–858.

Thome, K., Schiller, S., Conel, J., Arai, K., & Tsuchida, S. (1998). Results of the 1996 Earth Observing System vicarious calibration campaign at Lunar Lake Playa, Nevada (USA). *Metrologia*, *35*, 631–638.

Vane, G., Green, R. O., Chrien, T. G., Enmark, H. T., Hansen, E. G., & Porter, W. M. (1993). The airborne visible/infrared imaging spectrometer (AVIRIS). *Remote Sensing of Environment*, *44*, 127–143.

Vermote, E., Santer, R. P., Deschamps, P. Y., & Herman, M. (1992). In-flight calibration of large field of view sensors at short wavelengths using Rayleigh scattering. *International Journal of Remote Sensing*, *13*, 3409–3429.